

Applications and advances in polycapillary optics

C. A. MacDonald^{1*} and W. M. Gibson,^{1,2}

¹ Center for X-ray Optics, University at Albany, Albany, New York 12222, USA

² X-Ray Optical Systems, Inc., 15 Tech Valley Dr., East Greenbush, New York, NY 12061, USA

Received 24 July 2001; Accepted 4 February 2003

Polycapillary optics can be designed for a wide variety of x-ray applications. They have been used as focusing collectors for x-ray astronomy, to produce large-area collimated beams for wafer analysis and to provide small focused beams for protein crystallography with low-power x-ray sources. They are also being developed for a number of medical applications, including the removal of Compton scattering with the resultant improvement in contrast and resolution in mammography, the production of monochromatic parallel beams for high-contrast imaging in a clinical setting and the detection and localization of radioactive tracers in prostate cancer. Other exciting applications are extensions of measurements normally performed at synchrotrons into laboratory or clinical settings because of the increased efficiency of source utilization. The realization of these applications has been advanced by the recent marked improvement in available optic quality and reproducibility. Manufacturing progress has been assisted by the development of simulation analyses which allow for increasingly accurate assessment of optics defects. Optics performance over the whole range of energy from 10 to 80 keV can often be matched with one or two fitting parameters. This software development is ongoing, as is development of crystallographic analysis software designed to be used with highly focused beams. Continuing optics manufacturing challenges include the advance of applications at energies above 40 keV and the production of optics for imaging which are of adequate clinical size. Copyright © 2003 John Wiley & Sons, Ltd.

INTRODUCTION

Polycapillary x-ray optics are bundles of hollow glass capillary tubes.^{1–3} They differ from single-bore capillaries in that the capillary walls are thin to keep the fractional open area large. A cross-section of a polycapillary fiber is shown in Fig. 1. For polycapillary optics, focusing or collecting effects come from the overlap of the beams from thousands of capillary channels, rather than from the action within a single tube. As for single-bore capillaries, x rays can be transmitted down a curved hollow tube as long as the tube is small enough and bent gently enough to keep the angles of incidence less than the critical angle for total reflection, θ_c .⁴ As shown Fig. 2, the angle of incidence for the ray near one edge increases with tube diameter. The requirement that the incident angles remain less than the critical angle necessitates the use of tiny tubes. Polycapillary fibers have tube diameters that are much smaller than the fiber diameter, while still maintaining high open area. Typical channel sizes are between 2 and 12 μm . Thousands of such fibers are strung through lithographically produced metal grids to produce a multifiber lens, such as is shown in Fig. 3. Alternatively, a larger diameter polycapillary fiber can be shaped into a one-piece, monolithic optic, as shown Fig. 4. The development and study of polycapillary optics and its applications in x-ray

lithography,^{5,6} x-ray astronomy,^{7–9} diffraction analysis,^{10–16} x-ray fluorescence^{17,18} and medicine^{19–26} have been pursued since 1990.^{27–29}

In the last few years, there has been marked improvement in the quality of polycapillary optics, and also in the accuracy of the simulation analysis.¹ In the next three sections, defect analyses and applications studies of three types of optics, multifiber collimating, monolithic magnifying and monolithic focusing optics, are presented.

MULTIFIBER COLLIMATING OPTICS

Simulation analysis

Polycapillary fiber measurements and numerical simulations

Detailed measurements of polycapillary fibers, including transmission, absorption and exit divergence, have been performed as a function of length, bend radius, x-ray source position, x-ray source geometry and x-ray energy.^{27,28,30–33} Computer automated systems for fiber measurement have repeatability within 1%.³⁴ Extensive modeling programs used to describe the propagation of x-rays along capillaries with complex geometries have been developed. These computer codes are based on Monte Carlo simulations of geometrical optics trajectories and provide essential information on performance, design and potential applications of capillary optics. The geometric algorithm for the simulations is approximated in two dimensions by projecting the trajectory on to the local fiber cross-section.^{35,36} Reflectivities are computed³⁰ using optical constants from standard tables.^{37–39} The simulation also allows for the roughness^{40,41}

*Correspondence to: C. A. MacDonald, Physics Department, University at Albany, Albany, New York 12222, USA.
E-mail: c.macdonald@albany.edu
Contract/grant sponsor: NIH.
Contract/grant sponsor: NASA.
Contract/grant sponsor: DOD BCRP.

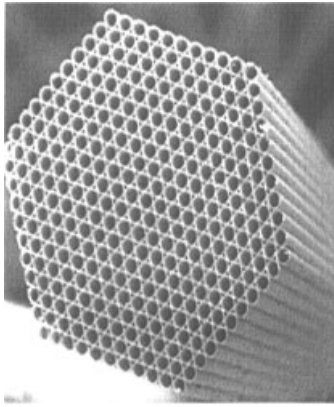


Figure 1. Cross-sectional scanning electron micrograph of a polycapillary fiber with 0.55 mm outer diameter and 50 μm diameter channels.

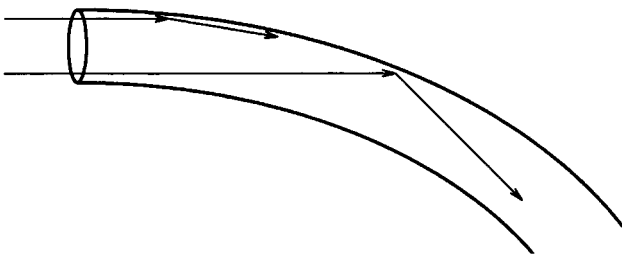


Figure 2. X-rays traveling in a bent capillary tube. The lower ray (entering close to the center of curvature) strikes at a larger angle.

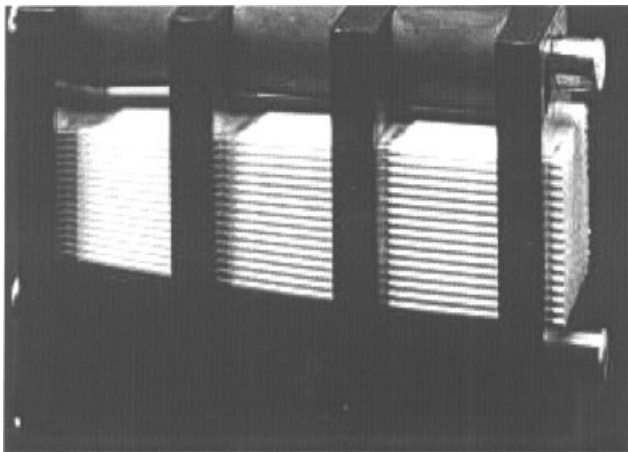


Figure 3. Multifiber collimating lens constructed from over 1000 individual polycapillary fibers strung through a series of four metal grids. The lens is 10 cm long with a 20 \times 20 mm output. The fibers are parallel at the output end (shown) and at the input end point to a common focal spot 15 cm from the entrance.

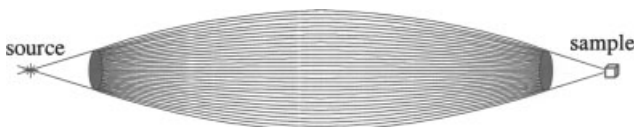


Figure 4. Sketch of the interior channels of a monolithic polycapillary optic. Monolithic optics can be focusing, as shown, or collimating, as in Fig. 3. Sketch adapted from Ref. 11.

and waviness^{33,42} of the capillary walls to be taken into account. Very good agreement is found between simulation and experimental results for a wide range of geometries.

Waviness. Capillary surface oscillations with wavelengths shorter than the capillary length and longer than the wavelength of the roughness are called waviness. The detailed shape of the channel walls is unknown, but waviness is modeled as a random tilt of the glass wall. The tilt angles are assumed to have a Gaussian distribution with width σ . For high-quality glass and photon energies less than 200 keV, σ is much smaller than the critical angle, θ_c . Consideration is taken in the simulation of the fact that the surface tilt angle will affect the probability of x-ray impact on that surface.⁴² The effect of waviness on fiber transmission is shown in Fig. 5.^{33,42} Waviness is primarily responsible for reduction of transmission at mid-range energies, and additionally for a reduction in the width of source scans at those energies. A simulation fit including waviness and bending for a single 0.5 mm diameter fiber with 10 μm channels is shown in Fig. 6.³³ Most borosilicate and lead glass optics have simulation fitting parameters which give a Gaussian width for the waviness of 0.12–0.15 mrad. This is in agreement with the slope error data of the Cornell group.⁴³

Blockage. Another defect that is seen occasionally in borosilicate glass optics, and more prevalently in lead glass fibers,³² is a drop in transmission at low energies, as shown in Fig. 7. Reasonable agreement is obtained over the whole range of photon energies by assuming that a glass layer of fixed thickness blocks the channels. The increase in required layer thickness with fiber length is consistent with a stochastic random model of glass inclusions. This random probability of glass inclusions would cause the transmission to drop exponentially with optic length, as shown in Fig. 8.

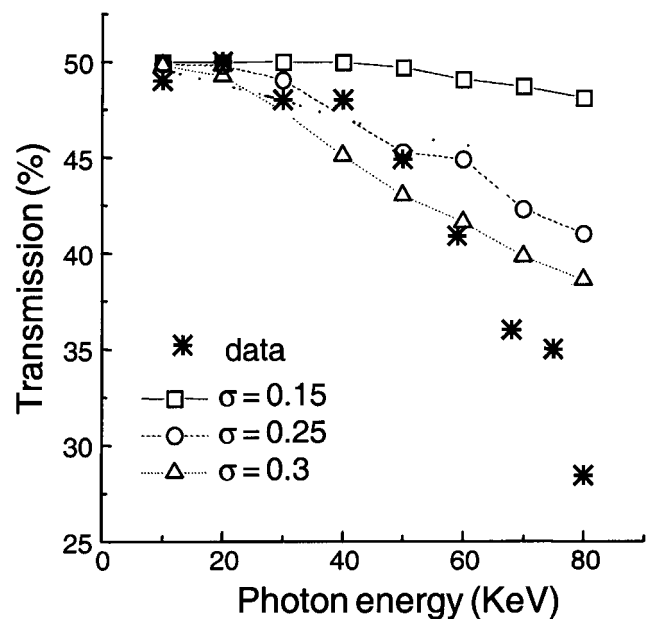


Figure 5. Simulations of transmission spectra for a fiber with waviness values from 0.15 to 0.3 mrad compared with the experimental data. The simulations do not include the roughness or bending. Adapted from Ref. 42.

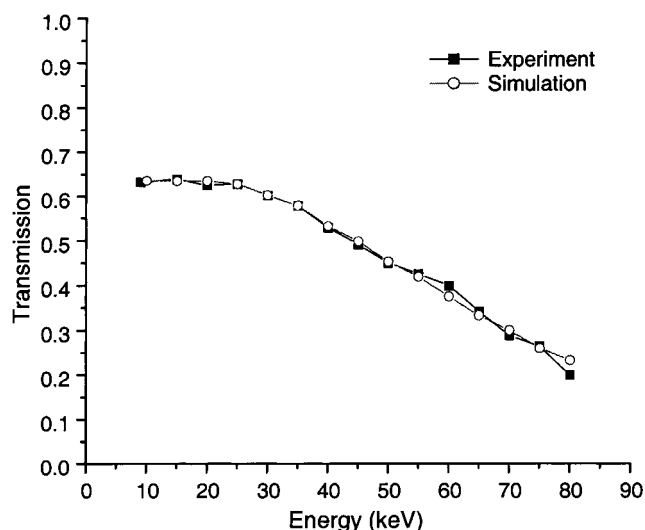


Figure 6. Transmission of a single fiber of the type used for the lens in Fig. 11(b), compared with simulation analysis with fitting parameters waviness = 0.15 mrad and unintentional central axis bending radius $R = 120$ m. From Ref. 47. Reproduced with permission from International Society for Optical Engineering.

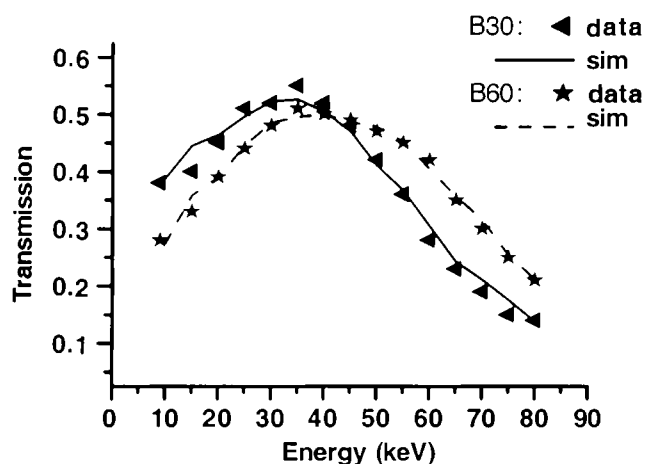


Figure 7. Transmission of two similar lead glass fibers, 30 and 60 mm in length. The simulation fits include 17 and 33 μm of glass layer, respectively, or 0.55 μm of blockage per mm of length. Adapted from Ref. 32.

Bending. Bending the channels increases the x-ray incidence angles, as shown in Fig. 2. Because the critical angle, θ_c , is inversely proportional to the x-ray photon energy,⁴ bending the channels decreases the x-ray transmission down the channels most significantly at higher photon energies. For the previously described measurements, the fibers were laid in grooves to be as straight as possible, although they suffered some unintentional bending. Deliberate bending measurements have also been performed using a simple mechanical apparatus,³⁰ for which results are shown as a function of angular deflection in Fig. 9,⁴⁴ or using a more elaborate system designed to mimic multifiber lenses,⁴⁵ shown as a function of photon energy in Fig. 10. In both cases, there is good agreement between known curvatures and simulation fits. The simulation allows for

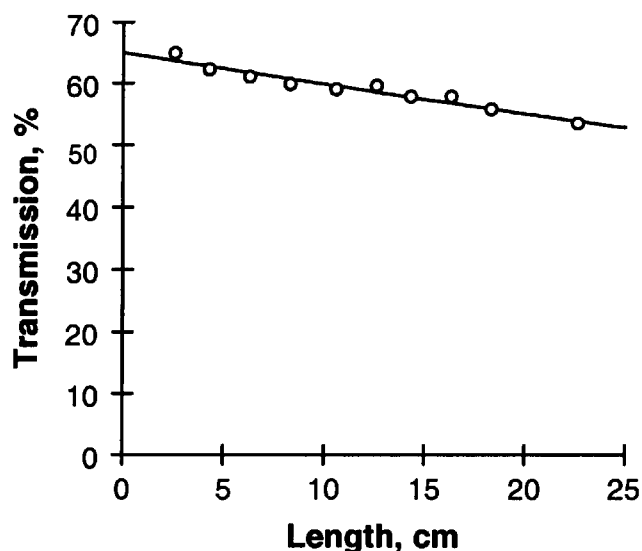


Figure 8. Measured transmission at 8 keV, as a function of length, for an older borosilicate polycapillary fiber with 17 μm channels. The solid line is an exponential fit with a decay length of 120 cm. That would be consistent with a glass inclusion thickness of approximately 1.1 μm per cm of optic length. Adapted from Ref. 20.

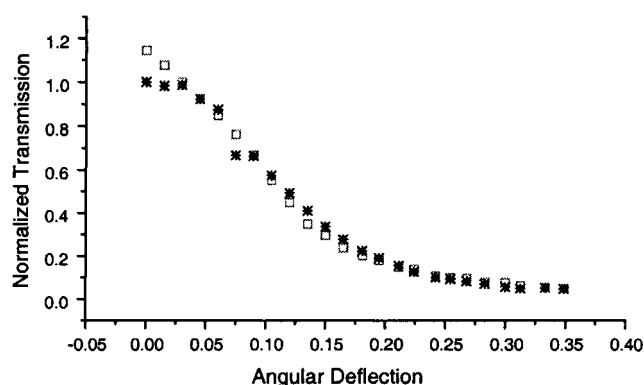


Figure 9. Measured (*) and simulated (\square) transmission as a function of deflection angle, in radians, for uniform circular bending at 8 keV. From Ref. 44.

accurate lens design. Using the simulations, lenses can be designed to have curvatures which deliberately discriminate against high photon energies, for example to enhance monochromaticity.

Lens quality analysis

The output image of an older collimating lens is shown in Fig. 11(a). Despite the occasional blocked channels from the relatively poor quality glass, most of the measured non-uniformity, as shown in Fig. 12, is a result of the drop in transmission at the outer edges of the lens due to the increased bending required of the off-axis fibers to keep the entrance ends directed toward the focal point.⁵⁷ The output non-uniformity was less than 6% for the central 20 mm of the optic.⁴⁸ Some reduction in transmission is due, in addition to fiber defects, to the effects of fiber misalignment, either due to manufacturing or to years of rough handling. This can be seen in the measurements, shown in Fig. 13, of transmission

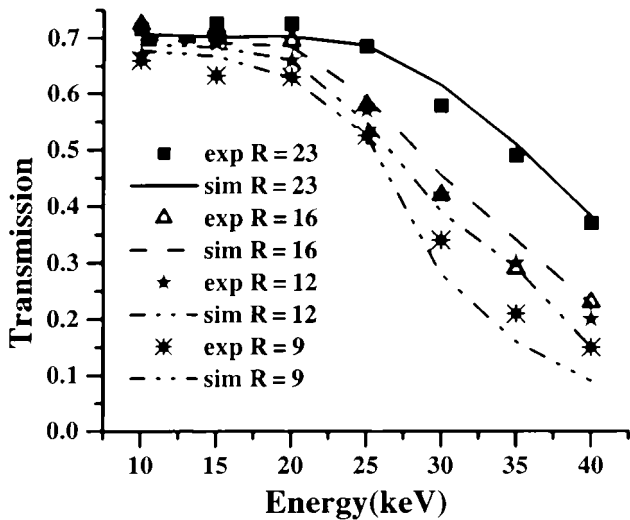


Figure 10. Simulated and experimental transmission for a fiber bent by deliberately displacing fiber holding screens of the kind used in a multifiber lens. The lines are simulated data with waviness $w = 0.12$ mrad, roughness $z = 0.65$ nm and different bending radii, R . Adapted from Ref. 45.

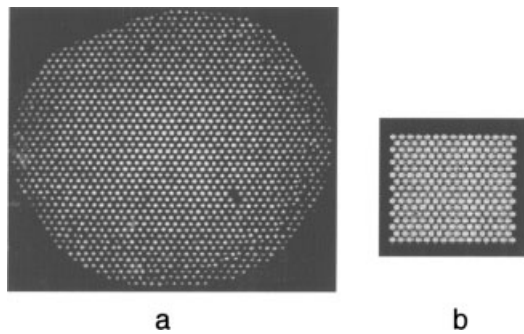


Figure 11. Images of x-ray output of (a) an older 3×3 cm lens with a 15 cm focal length, designed for 8 keV, and (b) a newer 1×1 cm lens with a 25 cm focal length, designed for 20 keV.

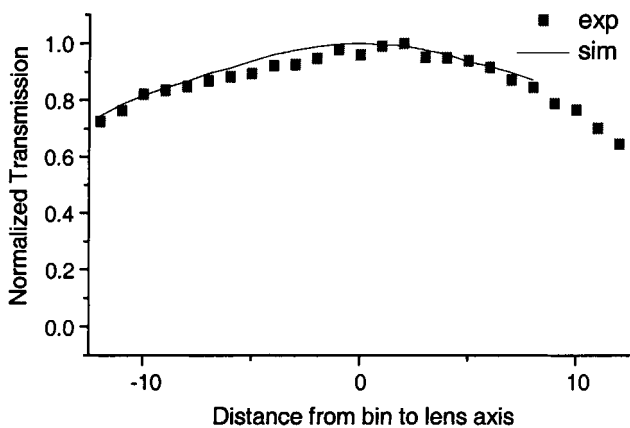


Figure 12. Measured and simulated local transmission of the lens in Figure 11(b), at 8 keV. The uniformity scan was carried out by scanning a 5×6 mm lead aperture across the output beam. Adapted from Ref. 42.

as a function of source location along the optic axis. The measured values of normalized transmission exceed the values expected from the simulation at short distances. This

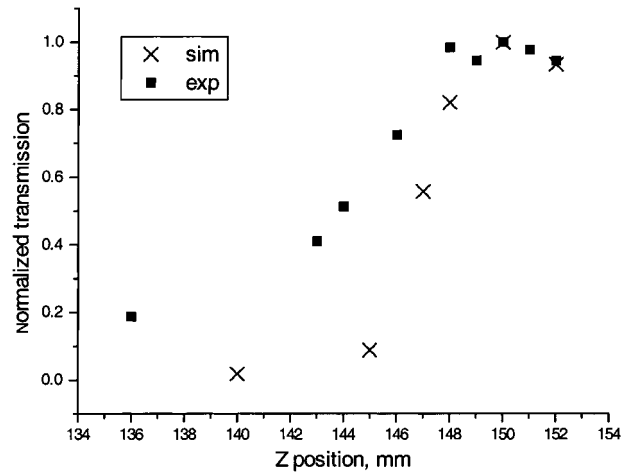


Figure 13. Variation in normalized measured (\square) and simulated (\times) transmission as the source is moved away from the lens along the fiber axis, for the lens in Fig. 11(a). Adapted from Ref. 44.

can be explained by fiber misalignment. Fibers that should be pointing at the focal spot are actually pointing slightly in front of the desired location, causing lower focal point transmission and higher transmission when the source is off the focal spot.⁵⁵

Fiber misalignment on the other side of the lens, at output, can be seen in the output divergence of the lens.^{47,55} The divergence was measured by placing a pinhole at different positions across the output of the optic before diffracting the beam off the crystal. The crystal was rotated to scan the (400) Bragg reflection for Cu $K\alpha$ radiation. Since the Darwin width of the silicon rocking curve is very much smaller than the measured divergence of the x-rays, the contribution of the crystal to the rocking curve can be neglected. Figure 14 shows the measured local divergence of the output of the collimating lens at 8 keV with the aperture at five different locations relative to the axis of the lens. The peak centers of these local divergence curves are systematically shifted. This shift could be caused by the output directions of the ends of the fibers being slightly convergent rather than parallel. An output image, taken at some distance from the lens, showed slight focusing.⁵⁵

In Fig. 14, the FWHM of each divergence curve is in the range of 3.8–3.9 mrad, very close to the critical angle of

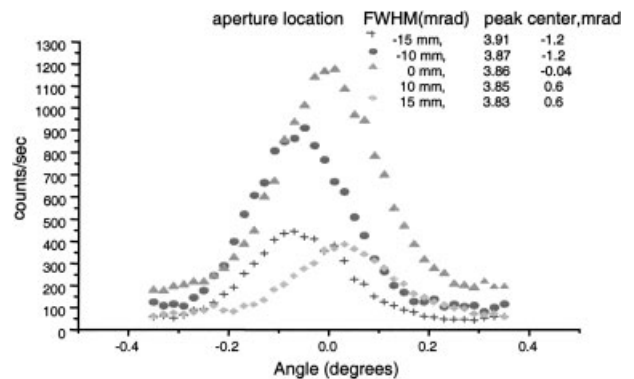


Figure 14. Measured local divergence of the output of the lens in Fig. 11(a) at 8 keV. Adapted from Ref. 46.

about 4 mrad at 8 keV, but much larger than the 2.5 mrad predicted by an ideal lens simulation. The divergence of the modeled ideal lens is low because the nearly straight central fibers, if ideal, would have an exit divergence of 2.4 mrad, equal to the input divergence determined by the source spot size. However, waviness increases the angle of reflection for x-ray photons for most bounces inside the channel and thus the average angle at which they exit the fiber. The simulated divergence of a straight fiber with a waviness of 0.15 mrad is 3.9 mrad, close to the local divergence of the lens. The increased divergence of real lenses, compared to ideal models, can be explained by waviness.⁴⁴

A more recent long focal length lens⁸ had no systematic shifts in local divergence, indicating that there was no systematic fiber misalignment. The average value for the divergence at 17.5 keV was 1.2 mrad, slightly less than the critical angle at that energy.⁴⁵ The uniformity of newer lenses is also good. The output of a newer lens designed for 20 keV is shown in Figure 11(b). The non-uniformity was less than 3% at 8 keV. The transmission of that lens as a function of photon energy is shown in Fig. 15.⁴⁷ Using the waviness and bending determined from the single fiber simulation of Fig. 6, the simulation fits the measured value well. This implies that other effects, such as fiber misalignment or blocked channels, are minimal.

The simulations shown in Figs 6 and 15 did not include roughness. Roughness decreases only slightly the specular reflectivity at low angles, and so has almost no impact on the transmission spectra there or in Fig. 15, but becomes increasingly important under circumstances in which the angle and number of reflections increase. It can be seen that surface roughness must be considered to model the effects of moving the source away from the focal point, as shown in Fig. 16. However, fiber misalignment effects as were seen in the older lens in Fig. 13 were not important for this lens.

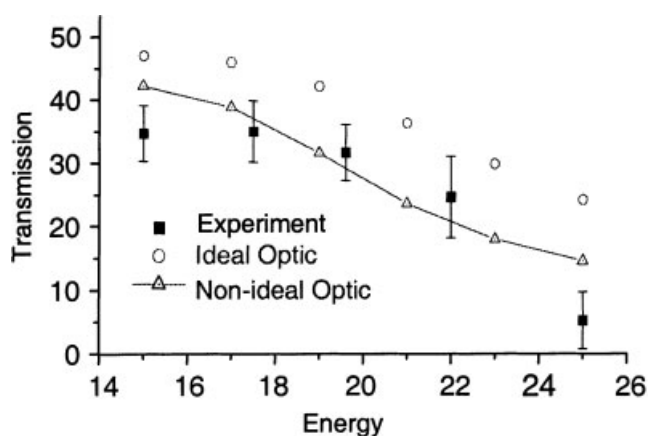


Figure 15. Comparison of experimental and simulated transmission as a function of energy for the lens in Fig. 11(b). The non-ideal simulation includes a waviness of 0.15 mrad and an unintentional bend with a radius of 125 m for the center fibers. From Ref. 47. Reproduced with permission from International Society for Optical Engineering.

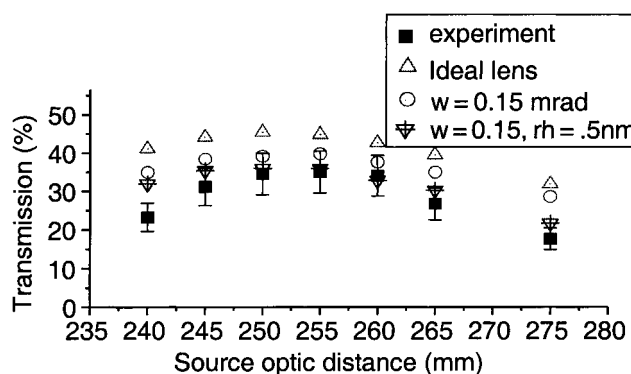


Figure 16. Measured and simulated transmission as the source is moved along the optic axis for the 25 cm focal length lens in Fig. 11(b) at 20 keV. The simulation with a waviness with a Gaussian width of 0.15 mrad fits the data when the source is at the focal point of 250 mm. Roughness with rms height of 0.5 nm is additionally required to fit the data at large displacements of the source.

Applications of multifiber collimating lenses

Multifiber collimating optics produce a large-area parallel beam from a conventional point source.

Large area diffraction

Gain: thin-film measurements. Because collimating optics efficiently redirect photons into a more parallel beam, they increase the intensity which will be diffracted from a crystal. This is particularly important for small samples, which will be discussed later, or for thin films. Measurements of thin films on wafer size substrates are especially well suited to multifiber lenses. Matney *et al.* have reported on measurements with a 3 cm diameter lens on a complex multilayer magnetic film with very thin interlayer thickness.⁴⁸ Intensity increases of more than two orders of magnitude with signal-to-background ratio improvement of more than an order of magnitude were obtained, as shown in Fig. 17. The measured gain is in agreement with simple geometrical calculations.¹²

Parallel beam advantages. An important reason to use a collimating optic, aside from intensity gain, is that a parallel beam geometry provides insensitivity to sample preparation, shape, position and transparency. An example of the insensitivity to sample position was reported by Bates⁴⁹, and is shown in Fig. 18, which shows a silicon powder diffraction peak measured with and without a polycapillary optic for different sample positions.¹⁴ Second, the symmetric beam profile and enhanced flux give much improved particle and measurement statistics. The constant peak width and resolution throughout the diffraction space facilitate very high precision residual stress and texture analysis and reciprocal space mapping.⁴⁸ The peak shape is ideally suited to phase identification and full pattern analysis of crystalline phase content using wavelet transforms. The parallel beam geometry also greatly simplifies alignment.¹⁰

Practical monochromatic mammography

Mammography has proven to be the single most effective means of reducing breast cancer mortality.⁵¹ Screening

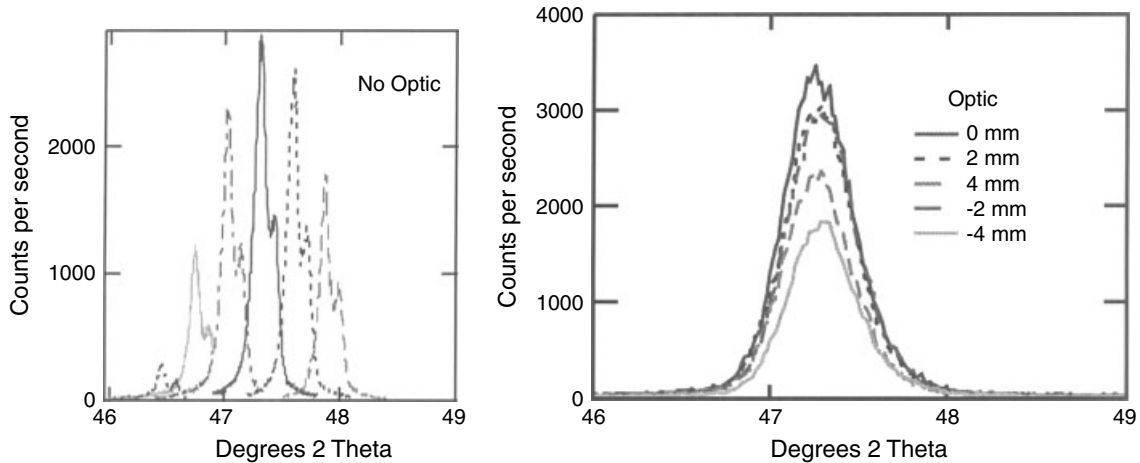


Figure 18. Silicon powder diffraction peak shift due to sample displacement with no optic (Bragg–Bretano geometry), left, and with a polycapillary collimating optic (parallel beam), right. Note in addition to the peak shift, in the Bragg–Bretano case the peaks are asymmetric due to the presence of the copper $K\alpha$ doublet. The resolution of the system in both cases was limited by the monochromator. Courtesy of Simon Bates, Kratos Inc.

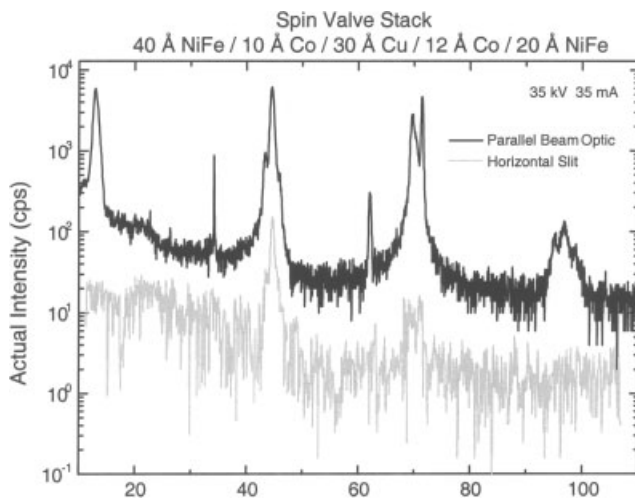


Figure 17. Spin valve stack. 40 Å NiFe/10 Å Co/30 Å Cu/12 Å Co/20 Å NiFe. The upper dark line is measurements with optic; the lower gray line is with horizontal slit and equal counting time. Note log intensity scale. Thin film peaks at 10, 30, 65 and 100° are not apparent without the optic. Adapted from Ref. 48.

mammography is an extremely challenging application of x-ray imaging, where dose, contrast, resolution, and cost are all critically important. The already low subject contrast is further reduced in a conventional system by averaging over relatively large energy bandwidths. Synchrotron measurements using monochromatic beams have demonstrated higher contrast, but synchrotrons are not clinically available. Using monochromator crystals with a conventional source without an optic is not practicable because the low intensity of the diffracted beam will not allow imaging *in vivo* before motion blur occurs. Polycapillary collimating optics can allow sufficient diffracted beam intensity to make clinical monochromatic imaging possible without a synchrotron. Because the monochromatization is done before the patient, the patient is only subjected to those x-rays which will contribute to the highest contrast image. Patient dose is reduced

because of the removal of low-energy photons that are heavily absorbed in the patient without contributing to contrast, and of high-energy photons that give relatively low subject contrast and that cause Compton scattering.

A preliminary test study using a 1 × 1 cm multifiber optic²³ demonstrated the use of polycapillary optics to produce monochromatic images from phantoms. A schematic of the contrast phantom, and the resulting images, are shown in Figs 19 and 20. The measured contrast of the 6.6 mm step was a factor of 5 higher for monochromatic 8 keV x-rays than for the polychromatic case. Similar enhancements were seen for phantoms with compositional variation. Preliminary measurements with a very low power source at 17.5 keV showed subject contrast enhancement of a factor of 2, also in agreement with theoretical calculations. This

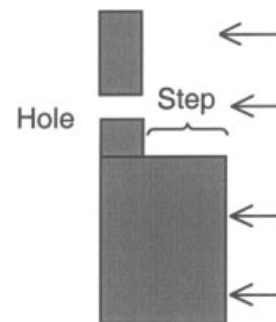


Figure 19. Shape of the polypropylene step phantom used for Fig. 20.

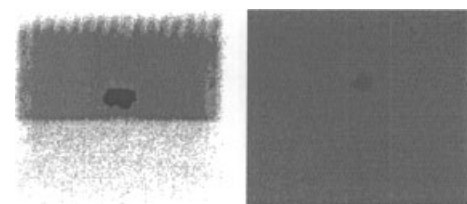


Figure 20. X-ray image of phantom, with 6.6 mm step, obtained with monochromatic beam (left), and conventional beam (right). Adapted from Ref. 23.

contrast enhancement is in addition to that expected from the reduction of scattered radiation.

Contrast in medical imaging is also significantly degraded by the presence of photons that have been Compton scattered out of the primary beam. The parallel beam produced by the crystal would allow removal of scattered radiation by introducing a simple air gap between the patient and the detector. With conventional tube sources, allowable air gap sizes are limited by geometrical blurring due to the finite source size, as shown in the top of Fig. 21. Implementation of a parallel beam would reduce geometrical blur and therefore allow a large air gap.

The output divergence of the collimating optic affects the resolution and is an important parameter especially for low-energy and high-resolution modalities. For the preliminary test measurement, good angular resolution was achieved even with a large spot source.

Resolution was measured by recording a knife edge shadow with a restimable phosphor computed radiography image plate. The derivative of the intensity profiles gives the angular distribution of the lens output. The Gaussian width of the output is given in Table 1 for silicon and mica crystals. For a perfect crystal and parallel monochromatic input beam, the knife-edge image would be ideally sharp (with a perfect detector). For a crystal with a large bandwidth, such as graphite, the angular width is determined by the

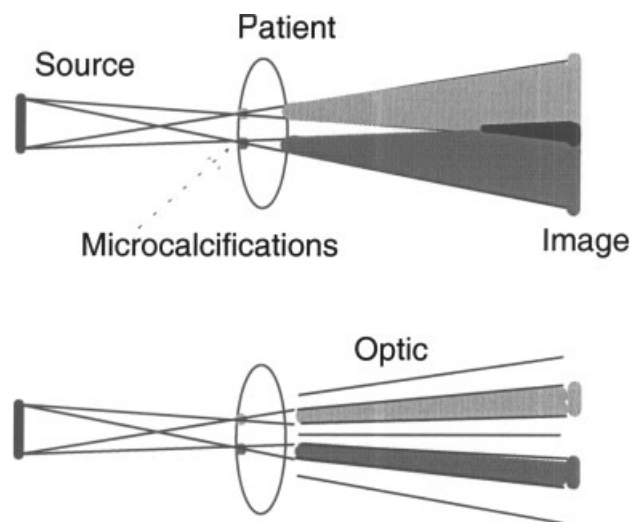


Figure 21. Air gap magnification (top) showing degradation of image due to finite source size. Magnification with a long tapered polycapillary optic (bottom) showing no increased blurring after the exit plane of the patient.

Table 1. System angular resolution using a polycapillary lens and three different crystals (from Ref. 23)

Crystal	Crystal bandwidth (mrad)	System resolution, data (mrad)	System theory (mrad)
Silicon	0.02	0.5 ± 0.2	0.3
Mica	0.3–0.5	0.8 ± 0.2	0.5–0.6
Graphite	35–87	6.5 ± 0.5	4.5

optic divergence, since the crystal can accommodate the full range of angles output from the optic. For a crystal with a bandwidth narrower than the optic divergence, a monochromatic beam would give a width equal to the crystal bandwidth. Thus, for the nearly perfect silicon crystal, the width results primarily from the energy spread of the incident radiation. The images showed the resolved Mo $K\alpha$ energy doublet. The 3 eV energy width of the $K\alpha_2$ emission line produces an angular spread of

$$\sigma_E \equiv \tan \theta_0 \frac{\sigma_{K\alpha_2}}{E_{K\alpha_2}} \approx 0.4 \text{ mrad} \quad (1)$$

Combining the effects of the crystal, lens divergence and energy spread, the angular distribution of intensity off the crystal can be approximated as a Gaussian distribution:

$$I(\Delta\theta) = \int \int I(\varphi) I(E(\beta)) p(\beta) \delta(\Delta\theta - \varphi + 2\beta) d\beta d\varphi dE \\ = \frac{\alpha}{2\sqrt{\pi}\sigma_{\text{optic}}\sqrt{\alpha^2 + \sigma_E^2}} e^{-\frac{\Delta\theta^2}{\sigma^2}} \quad (2)$$

where $\Delta\theta$ is the deviation of the output angle from the normal Bragg angle, $I(\varphi)$ is the angular distribution from the optic, assumed to be a Gaussian of width σ_{optic} , $I(E)$ is the spectral distribution of the $K\alpha_2$ line, also assumed Gaussian of width σ_E , and $p(\beta)$ is the probability distribution of planes at angle β from the surface of the crystal, assumed to have a Gaussian width α given by the crystal bandwidth. The delta function insures that the incidence angle equals the reflection angle. By making small angle approximations and completing the square, the integral can be performed analytically to give the output width:

$$\sigma = \sqrt{\frac{4\sigma_E^2\alpha^2 + \sigma_E^2\sigma_{\text{optic}}^2 + \sigma_{\text{optic}}^2\alpha^2}{\alpha^2 + \sigma_{\text{optic}}^2 + \sigma_E^2}} \quad (3)$$

The theoretical width is additionally broadened in quadrature by the detector resolution which is 50 μm at 300 mm or 0.2 mrad. The calculations are shown with the experimental angular resolutions, which are taken as the widths of the knife edge profiles, in Table 1. The values agree fairly well with the calculated resolutions.

The efficiency η of a crystal is calculated to be

$$\eta = \int I(\Delta\theta) d\Delta\theta = \frac{\alpha}{\sqrt{\sigma_{\text{optic}}^2 + \alpha^2 + \sigma_E^2}} \quad (4)$$

The intensity reflected by the crystal is η multiplied by the reflectivity, R , of the crystal itself. For silicon, the calculated η is 0.005, R is approximately unity and the measured efficiency is 0.003 ± 0.001 . Mica, with a larger bandwidth, α , gives a much higher efficiency, but similar resolution, since the resolution is limited not by α but by the energy width of the line. Hence mica should be preferable to avoid motion artifacts.

MONOLITHIC MAGNIFYING SCATTER REJECTION OPTICS

Introduction

As mentioned in the previous section, contrast is degraded by scattered radiation. In a conventional polychromatic medical

imaging system, scatter is partially removed by inserting a grid with lead ribbons parallel to the incoming beam. Alternatively, scatter can be removed by inserting a capillary optic between the patient and the detector. Because capillary optics have an angular acceptance that is limited by the very small critical angle (1.5 mrad at 20 keV), scattered photons are not transported down optics channels, but are largely absorbed by the glass walls of the capillary optic. Measured transmissions for scattered photons are typically less than 1%. This leads to measured contrast enhancements of around a factor of two for energies from 20 to 40 keV.^{19,45}

The tested prototype optics were also tapered and elongated to provide image magnification, as shown in Fig. 21. Using a prototype optic with a magnification of 1.8 the resolution was increased by the same factor of 1.8.¹⁹ Further, the modulation transfer function (MTF) was increased at all spatial frequencies, including the diagnostically important lower frequencies, as shown in Fig. 22.¹⁹ The resolution was not degraded by the capillary structure, which was on a smaller scale (20 μm channel size) than the desired resolution. The results were very promising, but the early optics suffered from low transmission efficiency.

Taper defect analysis

Studies were performed on a poorly transmitting optic to investigate the distributions of defects that were diminishing transmission.⁴⁷ The transmission of the optic and of its two halves after cutting are shown in Fig. 23. The final piece, A, was cut into three pieces, A1, which was 11 cm long, and A21 and A22, which were both 5.5 cm long. The defect localization into A21 is shown by the image and transmission measurement of Fig. 24. The transmission of the defected piece is higher at 24 keV than at 20 keV, which is the reverse of what is expected from the variation of critical angle with energy. The transmission dip could be due to glass blockages in the channels, which would be more transparent at higher energies. The competition between the increasing penetration of the blockages and the decreasing channel transmission with increasing energy produces a transmission

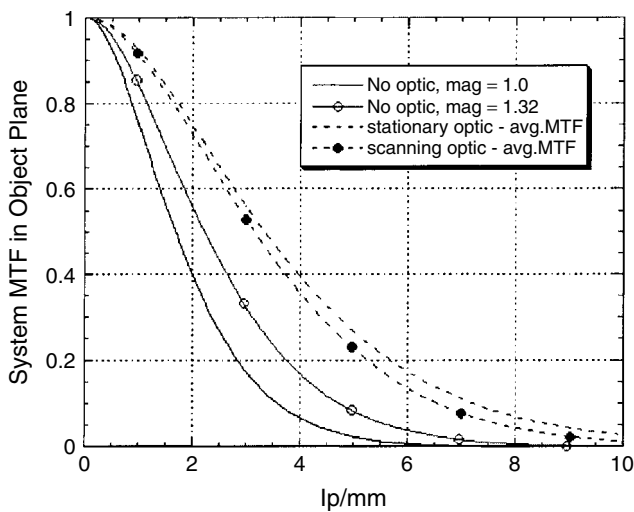


Figure 22. System MTF with and without optics. Adapted from Ref. 19.

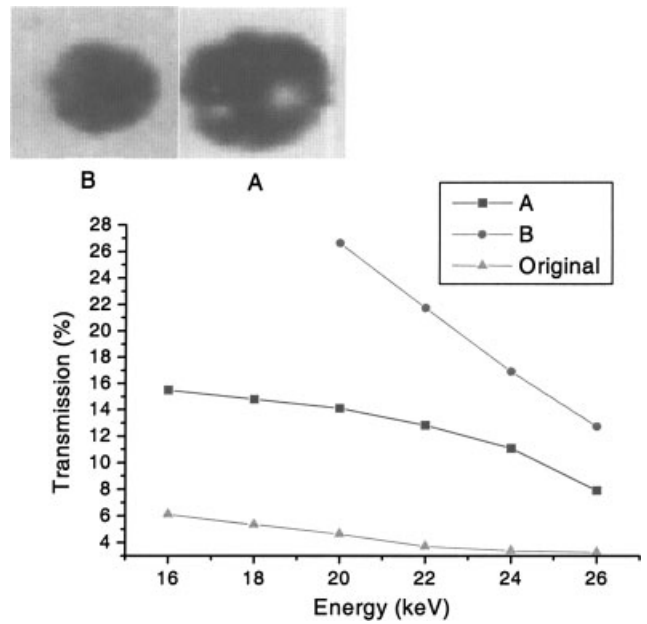


Figure 23. Transmission of original optic compared to two pieces. B is the first 10 cm (closest to the source), A is the final 22 cm.

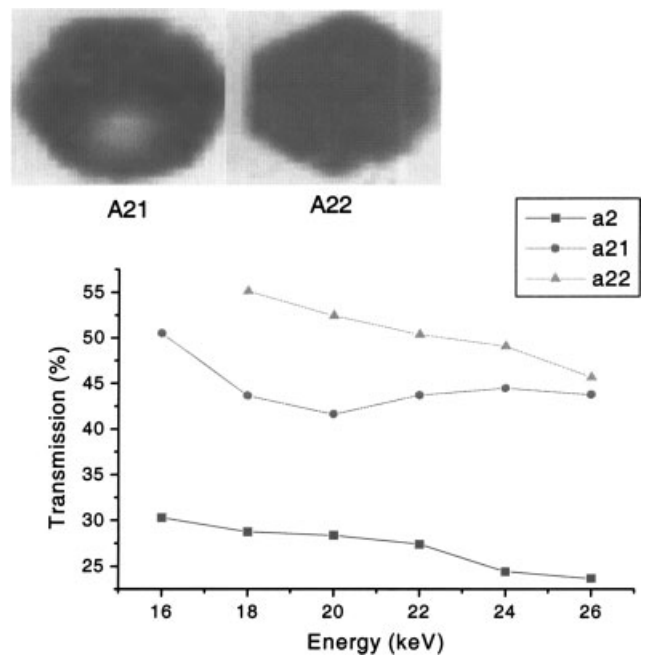


Figure 24. Transmission of final half of A (A2), and its two constituent pieces, the first 5.5 cm, A21 and the final 5.5 cm, A22. A21, shown as the left inset, contains a defect.

minimum. The effects of channel blockages were also seen in Figs 7 and 8.

Improvements

Partly as a result of the understanding developed from defect analysis, there have been significant advances in the manufacturing of long tapered monolithic optics. Transmission for seven tapers from a single recent batch is shown in Fig. 25. The transmission of all of the optics was greater than 40% at 20 keV. These were initial prototypes for placement in a

multioptic jig designed to increase the image area to a size which can be of clinical use.

Multioptic jig

Transmission measurements

Figure 26 shows a transmission image of three monolithic optics mounted together as a triad.⁵² The three individual optics have similar transmission and there is no leakage around the optics. The transmission of each optic was somewhat lower than when measured individually. This is due to the fact that the alignment was optimized for the group rather than any individual optic. Nonetheless the transmission is still fairly good (>44%) and is even fairly good when including the interoptic gaps (41%).

MTF measurements

The MTF of various pairs of optics are shown in Fig. 27.⁵¹ Simulation analysis showed that the optics must be aligned within 50 μm to keep the MTF degradation to less than 10% out to 3 lp mm⁻¹ and within 25 μm to keep the MTF degradation less than 6% out to 5 line-pair/mm.²⁵

Lead glass

For higher energy applications, or for cases where shorter optics are desirable, the scatter rejection optics should be

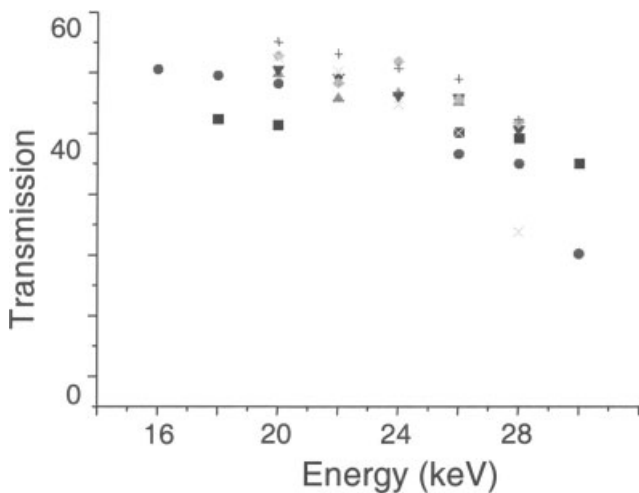


Figure 25. Transmission of seven 20 cm long tapered monolithic magnifying optics. Adapted from Ref. 47.

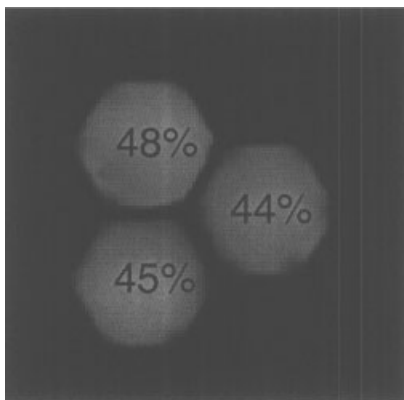


Figure 26. Transmission image of triad of monolithic optics. Adapted from Ref. 25.

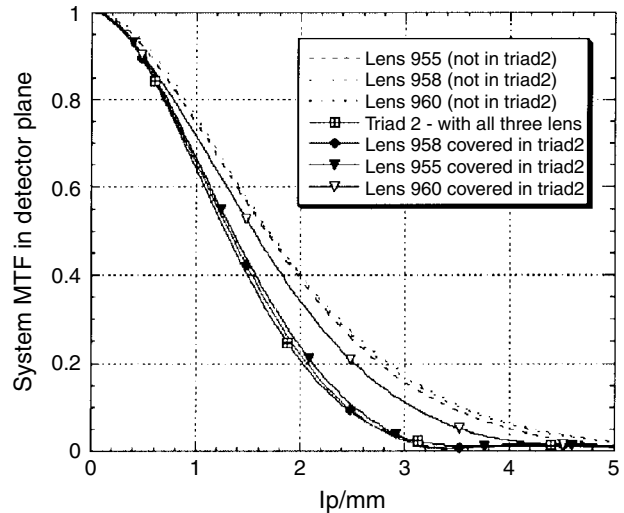


Figure 27. MTF of individual optics, the triad and optic pair. Adapted from Ref. 25.

made of lead glass.^{52,32} As shown in Fig. 7, lead glass fiber transmission is promising for short optics. Short lead glass scatter rejection optics could also be used for imaging radioactive sources, in a manner similar to gamma cameras.²⁶

MONOLITHIC FOCUSING OPTICS

Like the monolithic magnification optics, monolithic focusing optics have tapered channels. Focusing optics are designed so that the beams from each channel overlap at the output. This results in focal spot sizes that are limited only by the channel size and divergence from the channels. They can be considerably smaller than the optic diameter.

Focused beam diffraction theory

For focused beam diffraction, the volume of reciprocal space which is accessed in a single measurement is greatly increased compared with parallel beam geometries. The diffraction spot is not isotropically broadened by the convergence of the focused beam.^{12,13,15} Figure 28 displays a sketch of the diffraction condition for a single crystal with a monochromatic convergent beam. Diffraction conditions are satisfied for the two incident beam directions, k_0 and k_1 , when they make the same angle with the reciprocal lattice vector, G . Thus, changing the incident beam direction

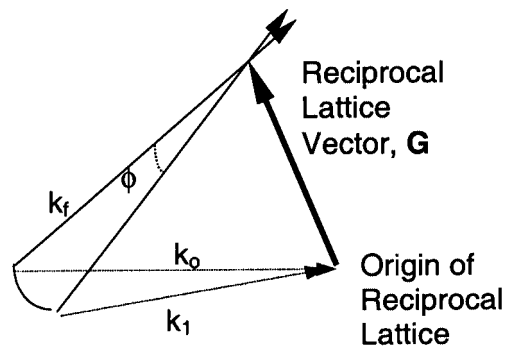


Figure 28. Ewald sphere description of focused beam diffraction on a single crystal.

Table 2. Comparison of protein crystallography data with and without a polycapillary optic with a 150 mm output focal length: both data sets were acquired on the same frozen chicken egg-white lysozyme crystal in 31 frames with a oscillation angle of 1.25° per frame, at 40 kV at 60 mA (Adapted from Ref. 15)

Parameter	With slightly focusing optic: Slightly focusing optic + 0.3 mm pinhole collimator + 12.5 μm Ni	Without optic: 0.3 mm pinhole collimator + 12.5 μm Ni
Time/frame (min)	4	30
Average intensity of reflections in common	10082 ± 491	3911 ± 255
PIN diode intensity of direct beam	2.0 × 10 ⁻³	1.0 × 10 ⁻⁴
Linear R-factor	0.069	0.064
Resolution (Å)	1.6	1.6

from k_0 to k_1 rotates the diffraction triangle of k_0 , G and k_f about the vector G by an angle ϕ . This results in the diffracted beam, k_f , moving to trace out a tangential line on the detector. There is no broadening in the radial direction. Comprehensive analysis programs for convergent beam protein crystallography have been developed and the first stages reported.⁵³ Protein diffraction patterns taken with smaller convergence can be analyzed with standard commercial software.

Protein results

A direct comparison was made of data quality and collection time on a rotating anode system using a single egg-white lysozyme crystal, with and without polycapillary optics.¹⁵ A description of the system and results is given in Table 2. The direct beam intensity gain and the diffracted beam signal gain were both a factor of 20 for a lens with a 0.3° convergence. There was no degradation in data quality.⁵⁵ The R-factor, which measures the similarity of the measured and model intensity for each diffraction, is defined as

$$R = \frac{\sum_{hkl} \|F_{obs} - s|F_{calc}\|}{\sum_{hkl} |F_{obs}|} \tag{5}$$

where F_{obs} and F_{calc} are the measured and theoretical structure factors for the (hkl) plane diffraction and s is a scale factor. Data was also taken with a low-power system.⁵⁴ The results, shown in Table 3, were of high quality and analyzed with conventional software, despite being taken with a source that was 100× less powerful than the rotating anode normally used.

CONCLUSIONS

Marked improvements in simulation accuracy and optic quality have emerged in the last 5 years. Systematic measurements allow the separate assessment of curvature, waviness,

Table 3. Protein crystallography data from a low power source: the polycapillary collimating optic was placed less than 10 mm from the small spot source, thus collecting from a much larger solid angle than for the experiment of Table 2 (from Ref. 54)

Parameter	Collimating optic + 500 μm pinhole collimator + 12.5 μm Ni
Sample	Chicken egg-white lysozyme at room temperature
Source setting	37 kV, 25 W
Oscillation angle (°)	1.5 (44 frames)
Time/frame (min)	60
PIN diode intensity	3 × 10 ⁻⁴
Resolution (Å)	1.99
R-factor (%)	5.15

roughness, channel blockage and channel misalignment on input and output. Improvements in optic quality have lead to practical implementation of many new applications and the potential development of a number of others. Microdiffraction using focused beams and high-contrast mammography are emergent new areas.

Acknowledgments

We acknowledge the measurements and analyses made by a large number of people, including D. K. Bowen, Dan Carter, Cari, Ning Gao, Mikhail Gubarev, Frank Hofmann, Joseph Ho, Huapeng Huang, John Kimball, Ira Klotzko, David Kruger, Kevin Matney, Charles Mistretta, Noor Mail, Scott Owens, Walter Pepler, Sushil Padiyar, Bimal Rath, Christine Russell, Francisca Sugiuro, Suparmi, Johannes Ullrich, Qi-Fan Xiao, Lei Wang, Hui Wang and M. Wormington. This work was supported in part by grant support from NIH, NASA and the DOD BCRP.

REFERENCES

- MacDonald CA, Gibson WM. In *Handbook of Optics*, vol. III, Bass M (ed). McGraw-Hill: New York, 2000; 30.1–30.12.
- Arkadev VA, Kolomitsev MA, Ponomarev IYu, Khodeev IA, Chertov YuP, Shakpsaranov IM, Kumakhov MA. *Sov. Physics. Usp.* 1989; **32**: 271.
- MacDonald CA. *J. X-Ray Sci. Technol.* 1996; **6**: 32.
- MacDonald CA, Gibson WM. In *Handbook of Optics*, vol. III, Bass M (ed). McGraw-Hill: New York, 2000; 19.1–19.10.
- Klotzko IL, Xiao QF, Gibson DM, Downing RG, Gibson WM, Karnaukhov A, Jezewski CJ. *Proc. SPIE* 1995; **2523**: 175.
- Turcu, ICE, Forber R, Grygier R, Rieger H, Powers M, Campeau S, French G, Foster R, Mitchell P, Gaeta C, Cheng Z, Burdett J, Gibson D, Lane S, Barbee T, Mrowka S, Maldonado JR. *Proc. SPIE* 1999; **3767**: 21.
- Russell CH, Gibson WM, Gubarev MV, Hofmann FA, Joy MK, MacDonald CA, Wang Lei, Xiao QF, Youngman R. *Proc. SPIE* 1997; **3113**: 369.
- Russell CH, Gubarev MV, Kolodziejczak J, Joy MK, MacDonald CA, Gibson WM. *Adv. X-Ray Analy.* 1999; **43**: (CD rom).
- Cari, MacDonald CA, Gibson WM, Alexander CD, Joy MK, Russell CH, Chen ZW. *Proc. SPIE* 2000; **4144**: 183.
- Kardiawarman, York BR, Qian XW, Xiao QF, MacDonald CA, Gibson WM. *Proc. SPIE* 1995; **2519**: 197.
- Owens SM, Hoffman FA, MacDonald CA, Gibson WM. *Adv. X-Ray Anal.* 1997; **41**: (CD rom).
- Hofmann FA, Gibson WM, Lee SM, MacDonald CA. *Mater. Res. Soc. Proc.* 1998; **505**: 3.

13. MacDonald CA, Owens SM, Gibson WM. *J. Appl. Crystallogr.* 1999; **32**: 160.
14. MacDonald CA, Gibson WM. In *Handbook of Optics*, vol. III, Bass M (ed). McGraw-Hill: New York, 2000; 35.1–35.37.
15. Hofmann FA, Gibson WM, MacDonald CA, Carter DA, Ho JX, Ruble JR. *J. Appl. Crystallogr.* 2001; **34**: 330.
16. Huang H, MacDonald CA, Gibson WM, Chik J, Parsegian A, Ponomarev A. *Proc. SPIE* 2001; **4502**: 30.
17. Gao N, Ponomarev IYu, Xiao QF, Gibson WM, Carpenter DA, *Appl. Phys. Lett.* 1997; **71**: 3441.
18. Hoffman FA, Gao N, Owens SM, Gibson WM, MacDonald CA, Lee SM. *Mate. Res. Soc. Proc.* 1998; **502**: 133.
19. Kruger DG, Abreu CC, Hendee EG, Kocharian A, Peppler WW, Mistretta CA, MacDonald CA. *Medi. Phys.* 1996; **23**: 187.
20. Abreu CC, MacDonald CA. *Phys. Med.* 1997; **13**: 79.
21. MacDonald CA, Gibson WM. *Proc. SPIE* 1995; **2519**: 186.
22. Fahrig R, Mainprize JG, Robert N, Rogers A, Yaffe MJ. *Med. Phys.* 1994; **21**: 1277.
23. Sugiro FR, MacDonald CA. *Proc. SPIE* 2001; **4320**: 427.
24. MacDonald CA, Sugiro FR, Gibson WM. *Proc. SPIE* 2001; **4502**: 10.
25. MacDonald CA, Gibson WM, Peppler WW. *Technol. Cancer Res. Treat.* 2002; **1**: 111–118.
26. Gibson WM, MacDonald CA, Mail N. *Proc. SPIE* 2002; **4781**: 104.
27. Gibson WM, MacDonald CA, Kumakhov MS. In *Technology Requirements for Biomedical Imaging*, vol. 2580 Mun SK (ed). IEEE Press, 1991; 164–169.
28. MacDonald CA, Abreu CC, Budkov S, Chen HH, Fu X, Gibson WM, Kardiawarman, Kamaukhov A, Kovantsev B, Ponomarev I, Rath BK, Ullrich JB, Vartanian M, Xiao XF. *Proc. SPIE* 1993; **2011**: 275.
29. Gibson WM and MacDonald CA. *Proc. SPIE* 1994; **2278**: 156.
30. Ullrich JB, Kovantsev V, MacDonald CA. *J. Appl. Phys.* 1993; **74**: 5933.
31. Abreu CC, Kruger DG, MacDonald CA, Mistretta CA, Peppler WW, Xiao QF. *Medi. Phys.* 1995; **22**: 1793.
32. Suparmi, Cari, Wang L, Wang H, Gibson WM, MacDonald CA. *J. Appl. Phys.* 2001; **90**: 5363.
33. Wang L, Rath BK, Gibson WM, Kimball JC and MacDonald CA. *J. Appl. Phys.* 1996; **80**: 3628.
34. Rath B, Youngman R, MacDonald CA. *Rev. Sci. Instrum.* 1994; **65**: 3393.
35. Xiao QF, Ponomarev IYu, Kolomitsev AI, Kimball JC. *Proc. SPIE* 1992; **1736**: 227.
36. Abreu CC. PhD. Thesis, University at Albany, 1994.
37. Henke BL, Gullikson EM, Davis JC. *At Nucl. Data Tables* 1993; **54**: 181.
38. Atomic Scattering Factors from the CXRO. www-cxro.lbl.gov/optical_constants.
39. X-ray Optical Constants from NIST. <http://physics.nist.gov/PhysRefData/XrayMassCoef/cover.html>.
40. Bittel D, Kimball J. *J. Appl. Phys.* 1993; **74**: 877.
41. Harve J. In *Handbook of Optics* Vol. II, Bassm (ed). McGraw-Hill: New York, 1996; chapt. 11.
42. Wang H, Lei W, Gibson WM, MacDonald CA. *Proc. SPIE* 1998; **3444**: 643.
43. Bilderbeck D, Fontes E. *AIP Conf. Proc.* 1997; **417**: 147.
44. Wang H. PhD Thesis, University at Albany, 2000.
45. Cari. PhD Thesis, University at Albany, 2001.
46. Gubarev M. PhD Thesis, University at Albany, 2000.
47. Sugiro FR, Padiyar SD, MacDonald CA. *Proc. SPIE* 2000; **4144**: 204.
48. Matney KM, Wormington M, Bowen DK, Xiao QF. *Adv. X-Ray Anal.* 1997; (CD rom).
49. Bates S. Presented at the European Powder Diffraction Conference 6, Budapest, 1998.
50. National Institutes of Health Consensus Development Panel. *J. Natl. Cancer Insti.* 1997; **89**: 1015.
51. Ross RE, Bradford CD, Peppler WW. *Med. Phys.* 2002; **29**: 1097.
52. Lei W, Gibson WM, MacDonald CA. *Proc. SPIE* 1999; **3767**: 102.
53. Ho JX, Snell EH, Sisk CR, Ruble JR, Carter DC, Owens SM, Gibson WM. *Acta Crystallogr., Sect. D* 1998; **54**: 200.
54. Huang H, MacDonald CA, Gibson WM, Carter DC, Ho JX, Ruble JR, Ponomarev I. *Proc. SPIE* 2000; **4144**: 100.
55. Padiyar SD, Gubarev MV, Wang H, Gibson MW, MacDonald CA. *Proc SPIE* 1999; **3767**: 90.